J Electroceram (2011) 27:93–107
DOI 10.1007/s10832-011-9635-x

FEATURE ARTICLE

Crystal chemistry and properties of mixed ionic-electronic conductors

Arumugam Manthiram · Jung-Hyun Kim · Young Nam Kim · Ki-Tae Lee

Received: 9 January 2011 / Accepted: 10 February 2011 / Published online: 24 February 2011

Abstract Oxides exhibiting mixed oxide-ion and electronic conducting (MIEC) properties have been attracting great interest in recent years due to their technological applications in solid-state electrochemical devices such as solid oxide fuel cells (SOFC), oxygen separation membranes, and electrochemical sensors. This article provides an overview of the composition-structure–property-performance relationships of several mixed conducting oxides: disordered ABO_3 perovskite oxides, A-site ordered layered $LnBaCo_2O_{5+\delta}$ (Ln = lanthanide) perovskite oxides, Ruddlesden-Popper series of perovskite-based $(La,Sr)_{n+1}M_nO_{3n+1}$ (n=1–3 and M = Fe, Co, and Ni) intergrowth oxides, and hexagonal RBa $(Co_{1-y}M_y)_4O_7$ (R = rare earth or alkaline earth and M = Zn) oxides. Based on the available data, the role of chemical composition, crystal chemistry, and chemical bonding on the electrical and ionic transport, thermal, and electrochemical properties is discussed.

Keywords Mixed ionic-electronic conductors · Metal oxides · Crystal chemistry · Electronic properties · Solid oxide fuel cells · Oxygen separation membranes

A. Manthiram (✉) · J.-H. Kim · Y. N. Kim · K.-T. Lee
Electrochemical Energy Laboratory & Materials Science and Engineering Program, University of Texas at Austin,
Austin, TX 78712, USA
e-mail: rmanth@mail.utexas.edu

Present Address:
K.-T. Lee
Division of Advanced Materials Engineering,
Chonbuk National University,
664–141 Deokjin-Dong,
Jeonju-City, Jeonbuk, Republic of Korea

1 Introduction

Transition metal oxides with mixed oxide-ion and electronic conducting (MIEC) properties find unique applications as electrode (cathode and anode) materials in solid oxide fuel cells (SOFC) and solid oxide electrolysis cells (SOEC) and as oxygen separation membranes. These applications require both high electronic and oxide-ion conductivities [1, 2] along with good structural and chemical stabilities [3] under the operating conditions of high temperatures (500–1000°C) and low or high oxygen partial pressures pO_2.

Transition metal oxides with perovskite or perovskite-related structures are the most widely investigated MIEC materials. For example, the $La_{1-x}Sr_xMnO_3$ (LSM) perovskite with acceptable thermal expansion coefficient (TEC), electronic conductivity, and chemical stability has been the leading cathode material for SOFCs operating at high temperatures (800–1000°C) [4, 5]. However, the high operating temperatures (>800°C) lead to thermal degradation and limitations in the interconnect materials. These problems have generated immense interest in reducing the operating temperatures to an intermediate level of 500–800°C. Unfortunately, the poor oxide-ion conductivity of LSM at these intermediate temperatures as Mn tends to remain as Mn^{4+} without creating any oxide-ion vacancies in the perovskite lattice limits its application in intermediate temperature SOFC (IT-SOFC). The poor oxide-ion conductivity also prevents its application as oxygen gas separation membranes. These difficulties have generated enormous interest in the development of alternative MIEC that can exhibit high oxide-ion and electronic conductivities as well as high catalytic activity for the oxygen reduction reaction (ORR) at intermediate temperatures.

In this regard, perovskite oxides containing cobalt such as $La_{1-x}Sr_xCoO_{3-\delta}$ (LSC) have become appealing due to

their high oxide-ion and electrical conductivity at intermediate temperatures, following the initial work by Teraoka et al. [6–8]. Among the various compositions investigated, the $SrCo_{0.8}Fe_{0.2}O_{3-\delta}$ sample exhibited the highest oxide-ion and electronic conductivities. However, it suffers from undesired phase transitions at high temperatures as well as huge TEC arising from high oxygen loss from the lattice and low-spin to high-spin transition with increasing temperature [8, 9].

Following the work on various $Ln_{1-x}Sr_xMO_{3-\delta}$ (Ln = lanthanide and M = Mn, Fe, Co, and Ni) perovskite oxides, perovskite-based layered $LnBaCo_2O_{5+\delta}$ oxides as well as Ruddlesden-Popper series of perovskite-based $(La, Sr)_{n+1}M_nO_{3n+1}$ (n=1–3 and M = Fe, Co, and Ni) intergrowth oxides have been widely investigated as MIECs and explored as cathodes in IT-SOFC or as oxygen separation membranes [10–20]. The crystal structure as well as the A or B-site cations play an important role in determining the MIEC properties of such perovskite and perovskite-related oxides. Based on the experimental data, several interesting relationships among structure, composition, and transport and catalytic properties have been established in the literature. For example, the Goldschmidt tolerance factor [21], critical radius for the dimension of oxide-ion pathway [22], lattice free volume [23, 24], and degree of lattice stress [25] have been proposed as key factors that govern the ionic conductivity. More recently, a new class of RBa $(Co,M)_4O_7$ (R = rare earth or alkaline earth and M = Zn) oxides based on a hexagonal structure have also been found to exhibit interesting MIEC properties [26].

Although there is no simple rule that can readily predict the MIEC properties of transition metal oxides, several trends in the MIEC properties can be established based on the vast experimental data available in the literature. Accordingly, this review provides an overview of the structure-composition-properties of several MIECs: disordered ABO_3 perovskite oxides, A-site ordered layered $LnBaCo_2O_{5+\delta}$ (Ln = lanthanide) perovskite oxides, Ruddlesden-Popper series of perovskite-based $(La,Sr)_{n+1}M_nO_{3n+1}$ (n = 1–3 and M = Fe, Co, and Ni) intergrowth oxides, and hexagonal RBa $(Co_{1-y}M_y)_4O_7$ (R = rare earth or alkaline earth and M = Zn) oxides. Specifically, the influence of chemical compositions on the crystal chemistry, thermal expansion coefficient, electronic and oxide-ion conductivities, and catalytic activity for ORR in SOFC is discussed.

2 ABO_3 perovskite oxides

Figure 1 shows the ideal cubic ABO_3 perovskite structure, in which the larger A^{n+} cation has a 12-fold oxygen coordination while the smaller B^{n+} cation has a six-fold (octahedral) oxygen coordination. The BO_6 octahedra share

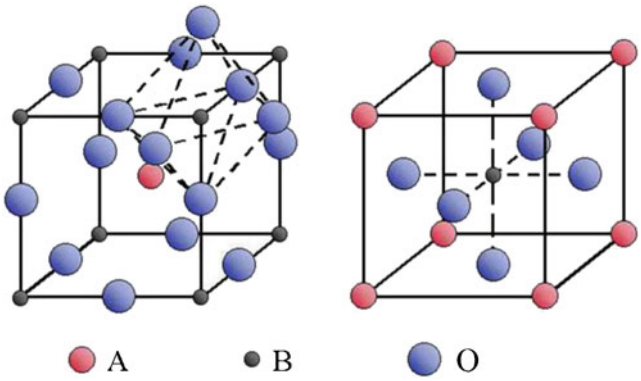

Fig. 1 Crystal structure of an ideal ABO_3 perovskite oxide

corners along the three crystallographic directions with a 180° B-O-B bonding. While the B^{n+} cations are in contact with the O^{2-} ions along the cube edge, the A^{n+} cations are in contact with the O^{2-} ions along the face diagonal. Thus, the atomic arrangements with cation-anion contacts in the ideal cubic perovskite structure of Fig. 1 result in a geometric constraint,

$$r_A + r_O = \sqrt{2}(r_B + r_O) \tag{1}$$

where r_A, r_B, and r_O are, respectively, the ionic radii of the A^{n+}, B^{n+}, and O^{2-} ions. However, the ionic radii of the A^{n+}, B^{n+}, and O^{2-} ions may seldom match to satisfy the above relationship in Eq. 1, so Goldschmidt [22] introduced a geometric parameter called tolerance factor t, which is defined based on Eq. 1 as

$$t = \frac{r_A + r_O}{\sqrt{2}(r_B + r_O)} \tag{2}$$

The value of t will be unity when the ionic radii values match ideally and deviate from unity when they do not match ideally. It has been observed that perovskite oxides are formed for $0.75<t<1.1$. The deviation of t from unity is accommodated by structural changes to lower symmetries such as orthorhombic and monoclinic [27] including a bending of the O-B-O bonds with a bond angle <180° to provide a matching to the O-A-O bonds. However, apart from the value of t, other factors such as degree of covalency, Jahn-Teller distortion, and the effect of lone pairs on the A^{n+} cations also play a role in controlling the structure [28].

In addition to the geometric relationship described above, maintenance of charge neutrality between the cations and anions is another important aspect. As alio-valent cationic doping in the A- or B-sites is often carried out to realize the desired properties, the charge neutrality is maintained either by creating anionic vacancies (ionic compensation mechanism) or by an oxidation/reduction of

the B^{n+} cations (electronic compensation mechanism) or by both the mechanisms. Furthermore, the oxidation states of the B^{n+} cations vary significantly with temperature and oxygen partial pressure as the higher oxidation states becomes less stable at higher temperatures and/or under low oxygen partial pressures pO_2. Accordingly, the oxygen content $3\pm\delta$ in $ABO_{3\pm\delta}$ varies significantly with temperature and pO_2, and formation of oxygen vacancies often occurs with increasing temperatures or decreasing pO_2, resulting in significant changes in the crystal chemistry and MIEC properties.

For instance, the oxygen content $3\pm\delta$ in $La_{1-x}Sr_xMnO_{3\pm\delta}$ (LSM) varies with pO_2 as shown in Fig. 2 [29]. At moderate pO_2 and temperatures, the oxygen content remains at the stoichiometric value of 3.0 with $\delta=0$ as Mn^{4+} is stable under these conditions, and the charge neutrality on substituting Sr^{2+} for La^{3+} in LSM is maintained by the electronic compensation mechanism as

$$LaMnO_3 \xrightarrow{xSr} La^{3+}_{1-x}Sr^{2+}_x Mn^{3+}_{1-x}Mn^{4+}_x O_3 \quad (3)$$

At high pO_2 and low temperatures, LSM incorporates excess oxygen with an oxygen content of $3+\delta$ as

$$La^{3+}_{1-x}Sr^{2+}_x Mn^{3+}_{1-x}Mn^{4+}_x O_3 \rightarrow La^{3+}_{1-x}Sr^{2+}_x Mn^{3+}_{1-x-2\delta}Mn^{4+}_{x+2\delta}O_{3+\delta} \quad (4)$$

However, accommodation of the excess oxygen in the interstitial sites is difficult in the perovskite structure, so a corresponding amount of cation vacancies is formed in the perovskite lattice to keep the oxygen content as 3.0 [2]. At very low pO_2 or high temperatures, the oxidation state of Mn in LSM decreases and the charge neutrality is maintained by the ionic compensation mechanism as

$$La^{3+}_{1-x}Sr^{2+}_x Mn^{3+}_{1-x}Mn^{4+}_x O_3 \rightarrow La^{3+}_{1-x}Sr^{2+}_x Mn^{3+}O_{3-0.5x} \quad (5)$$

However, the oxygen deficiency in LSM occurs at very low $pO_2<10^{-9}$ atm and in a very narrow pO_2 range [29].

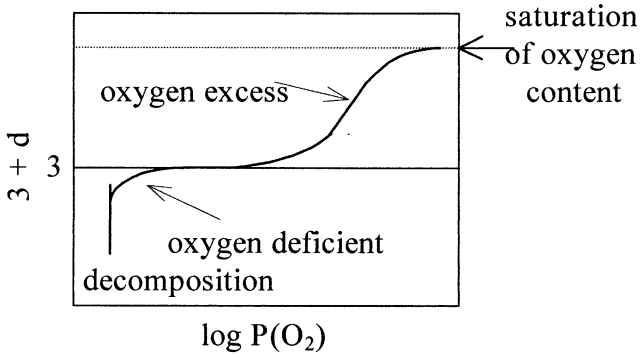

Fig. 2 Schematic profile of the variation of the oxygen content in $La_{1-x}Sr_xMnO_{3+\delta}$ with oxygen partial pressure pO_2 [29]

Further decrease in pO_2 results in a decomposition of the phase.

Often with the ABO_3 perovskite oxides, both the ionic and electronic compensation mechanisms tend to be present together depending on the temperature and pO_2. Generally, the electronic compensation mechanism dominates at high pO_2 and low temperatures while the ionic compensation mechanism dominates at low pO_2 and high temperatures. At a given temperature and pO_2, the occurrence of electronic vs ionic compensation mechanisms and the degree to which each of them occurs depend on the ABO_3 pervsikte system and the A^{n+} and B^{n+} cations. Also, oxide-ion vacancies are much more common compared to cation vacancies in the pervoskite oxide systems.

Similar to that in LSM, the substitution of Sr^{2+} for Ln^{3+} in $Ln_{1-x}Sr_xCoO_3$ (Ln = lanthanide) could be accommodated either by the oxidation of Co^{3+} to Co^{4+} (electronic compensation) as $Ln^{3+}_{1-x}Sr^{2+}_x Co^{3+}_{1-x}Co^{4+}_x O_3$or by the formation of oxide-ion vacancies (ionic compensation) as $La^{3+}_{1-x}Sr^{2+}_x Co^{3+}O_{3-0.5x}$. The electronic and ionic compensation mechanisms in $Ln_{1-x}Sr_xCoO_{3-\delta}$ also depend on the doping level x, oxygen partial pressure, and temperature. For example, the concentration of Co^{4+} in the air-synthesized $La_{1-x}Sr_xCoO_{3-\delta}$ system increases with x, reaches a maximum at $x\approx0.4$, and then decreases as reported by Petrov et al. [30]. These results reveal that the charge imbalance caused by Sr^{2+} substitution is accommodated primarily by the ionic compensation mechanism at higher doping levels ($x>0.4$) in $La_{1-x}Sr_xCoO_{3-\delta}$.

Additionally, the crystal chemistry of $Ln_{1-x}Sr_xCoO_{3-\delta}$ is strongly influenced by the size of the Ln^{3+} ions [31]. While the Ln = La sample adopts a rhombohedral structure, the Ln = Pr, Nd, Sm, and Gd samples have an orthorhombic structure. The lattice parameters, lattice volume, pseudo-cubic lattice parameter, and tolerance factor t for the $Ln_{0.6}Sr_{0.4}CoO_{3-\delta}$ samples are summarized in Table 1. As the ionic radius of the Ln^{3+} ion decreases, the pseudo-cubic lattice parameter a' and the Goldschmidt tolerance factor t decrease from Ln = La to Gd. The decreasing in t with the decreasing size of the Ln^{3+} ions is accommodated by a bending of the O–Co–O bond angle from the ideal value of 180° and a consequent lowering of the crystal symmetry as evidenced by the orthorhombic distortion.

Another perovskite oxide system that has attracted great interest in recent years is the $SrFe_{1-y}Co_yO_{3-\delta}$ system. The $SrFe_{1-y}Co_yO_{3-\delta}$ system accommodates a large degree of oxide-ion vacancies [32] compared to the $Ln_{1-x}Sr_xCoO_{3-\delta}$ (with low x) system due to the higher nominal oxidation state of $Fe_{1-y}Co_y$ in the former. Although the oxide-ion vacancies help to realize high oxygen permeability in $SrFe_{1-y}Co_yO_{3-\delta}$, the high concentrations of the oxygen vacancies tend to order, resulting in a structural transition from a disordered perovskite to an ordered $A_2B_2O_5$

Table 1 Lattice parameters, lattice volume, pseudo-cubic lattice parameter (a'), tolerance factor (t), and chemical analysis data of $Ln_{0.6}Sr_{0.4}CoO_{3-\delta}$ [31]

Ln	a (Å)	b (Å)	c (Å)	Lattice volume (Å^3)	a' (Å)	t	Oxidation state of Co	Oxygen content (3-δ)
La[a]	5.4079(4)	–	–	112.5	4.8274	0.965	3.38	2.99
Pr	5.3733(5)	5.4240(5)	7.5962(8)	221.4	3.8110	0.957	3.39	3.00
Nd	5.3656(5)	5.4148(4)	7.5917(7)	220.6	3.8064	0.953	3.38	2.99
Sm	5.3564(6)	5.3814(5)	7.5792(8)	218.5	3.7943	0.946	3.39	3.00
Gd	5.3578(9)	5.3654(4)	7.5718(8)	217.7	3.7897	0.941	3.40	3.00

[a] Rhombohedral cell angle, α=60.28°

brownmillerite structure. The latter structure consists of BO_6 octahedra alternating with BO_4 tetrahedra as seen in Fig. 3, in which oxide-ion vacancies are ordered in alternating (010) planes of the perovskite structure. For example, the $SrCo_{0.8}Fe_{0.2}O_{3-\delta}$ perovskite phase transforms to the $Sr_2Co_{1.6}Fe_{0.4}O_5$ brownmillerite phase with decreasing pO_2 at T<1,073 K [9, 10].

Some perovskite oxides exhibit good MIEC properties, making them attractive candidates for electrochemical devices such as SOFC electrodes and oxygen separation membranes. Especially, the cobalt-containing perovskite is of great interest due to their superior oxide-ionic and electronic conductivity values compared to those containing other 3d transition metal ions. In this regard, the structural-property relationships of the cobalt-based perovskite oxides have been explored intensively during the past few decades. As an example, the electrical properties of the $Ln_{1-x}Sr_xCoO_{3-\delta}$ are strongly influenced by their crystal chemistry. Figure 4(a) shows the variations of the total electrical conductivity of the $Ln_{1-x}Sr_xCoO_{3-\delta}$ system. At a given temperature, the electrical conductivity decreases with decreasing size of the Ln^{3+} ions from Ln = La to Gd. This can be understood by considering the changes in the structural parameters. As illustrated in Fig. 5, the decreasing tolerance factor t (Table 1) with decreasing ionic radius from La^{3+} to Gd^{3+} increases the bending of the O–Co–O bonds (lowers the O–Co–O bond angle from 180°), which results in a decrease in the overlap between the $Co^{3+/4+}$:3d and O^{2-}:2p orbitals and the bandwidth W [31]. Thus, the decreasing covalency of the Co–O bonds and the increasing electron localization from Ln = La to Ln = Gd cause a decrease in the electrical conductivity.

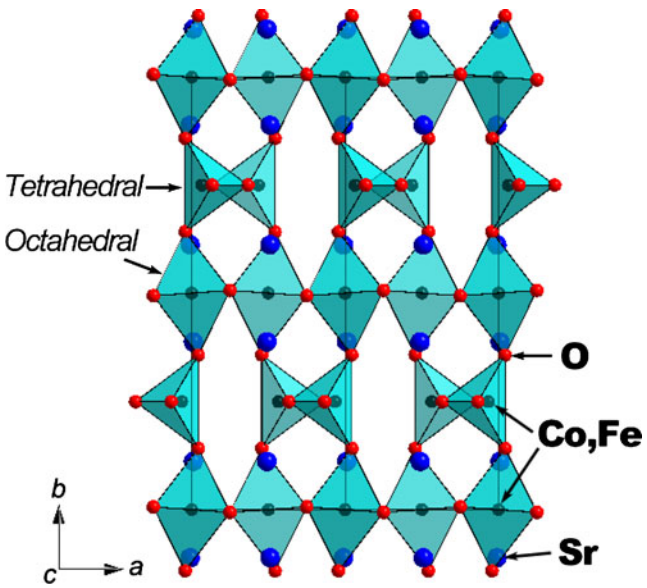

Fig. 3 Crystal structure of the $Sr_2(Fe_{1-y}Co_y)_2O_5$ brownmillerite

The effect of Sr content on the total electrical conductivity of $Nd_{1-x}Sr_xCoO_{3-\delta}$ is also shown in Fig. 4(b) [33]. At a given temperature, the electrical conductivity increases with Sr content due to an increasing Co^{4+} content and charge carrier concentration as well as an increasing Co-O cavalency resulting from a decreasing charge transfer gap between the Co^{4+}:3d and O^{2-}:2p bands. The conductivity increases with increasing temperature for x<0.3, implying a small polaron semiconductor behavior, but decreases with increasing temperature for x≥0.3, implying a metallic behavior. The $Nd_{1-x}Sr_xCoO_{3-\delta}$ system thus exhibits a semiconductor to metal transition around x=0.3. The faster decrease in conductivity at higher temperatures for samples with x≥0.3 in Fig. 4(b) is due to the loss of oxygen from the lattice at higher temperatures and the consequent decrease in the Co^{4+} content and charge carrier concentration and increasing carrier localization.

The oxygen permeability and ionic conductivity of the $LaCoO_3$-based perovskite membranes were first demonstrated by Teraoka et al. [6–8, 34]. The oxide-ion conductivity of such cobalt-based perovskite oxides were found to be 2–4 orders of magnitude higher than that obtained with the yttira stabilized zirconia (YSZ) at a given temperature. In addition, the oxygen permeability of the $La_{1-x}Sr_xCo_{1-y}Fe_yO_{3-\delta}$ membrane increased with the Sr content x [6]. This can be understood to be due to the increasing amount of oxide-ion vacancies caused by the ion-compensation mechanism on substituting a higher amount of Sr^{2+} for Ln^{3+}, which is beneficial for the bulk diffusion of oxide-ions. With good MIEC properties, the $Ln_{1-x}Sr_xCoO_{3-\delta}$ oxides have been

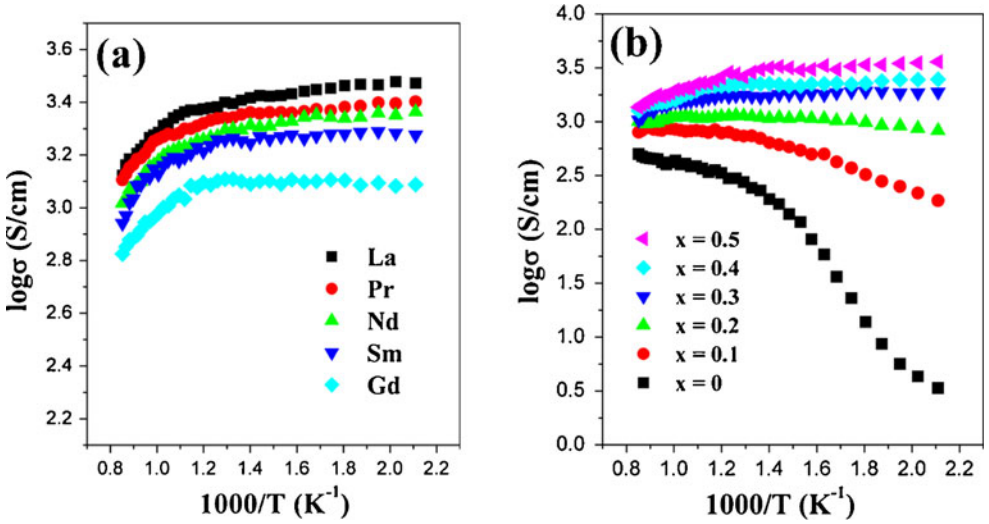

Fig. 4 Variations of the electrical conductivities of the (**a**) $Ln_{0.6}Sr_{0.4}CoO_{3-\delta}$ (Ln = La, Pr, Nd, Sm, and Gd) and (**b**) $Nd_{1-x}Sr_xCoO_{3-\delta}$ samples with temperature in air [31, 33]

intensively investigated as promising candidates for cathode materials in IT-SOFC and as oxygen separation membranes. With decreasing Ln^{3+} radius form Ln = La to Gd, the over-potential increases and the power density decreases in SOFC as seen in Fig. 6. The cathode over-potential can be affected by both the electronic and ionic conductivities because the electrocatalytic reaction at a porous cathode is controlled by the kinetics of oxygen exchange and diffusion as well as the charge transfer. This is supported by the literature data showing a decrease in both the electrical [31] and ionic conductivities [35, 36] from Ln = La to Gd in $Ln_{0.6}Sr_{0.4}CoO_{3-\delta}$. Kharton et al. [35] have suggested that the decreasing oxide-ion conductivity from La to Gd is because of a decrease in the anion transfer channel size as evidenced by the decreasing cell volume and an increase in the (Ln,Sr)–O bond energy.

Another important physical property requirement for an oxide to be employed as an electrode material in SOFC is the matching of the thermal expansion coefficient (TEC) with the TECs of the other fuel cell components such as the electrolyte and interconnect materials. As SOFC is an all-solid-state device operating at high temperatures, thermal expansion mismatch results in the delamination of the components during thermal cycling. In this regard, use of $La_{1-x}Sr_xCoO_{3-\delta}$ as a cathode in SOFC is challenging because of its much higher TEC value (21.3×10^{-6}°C^{-1}) compared to those of the standard electrolyte materials like YSZ, GDC, and LSGM (10.0×10^{-6}–12.5×10^{-6}°C^{-1}). The large TEC value of $Ln_{1-x}Sr_xCoO_{3-\delta}$ can be understood by considering the spin-state transition associated with the Co^{3+} ions. For example, the high TEC of the cobalt-containing perovskites (*e.g.* $LnCoO_3$) has been considered to be due to the transition of low-spin $Co^{III}\left(t_{2g}^6e_g^0\right)$ to intermediate-spin $Co^{iii}\left(t_{2g}^5e_g^1\right)$ or high-spin $Co^{3+}\left(t_{2g}^4e_g^2\right)$ [31, 37]. In addition, oxygen loss from the lattice with increasing temperature also contributes to the increase in TEC due to the reduction of the smaller Co^{4+} ions to larger Co^{3+} ions [30, 38]. The $Ln_{1-x}Sr_xCoO_{3-\delta}$ oxides exhibit a decrease in

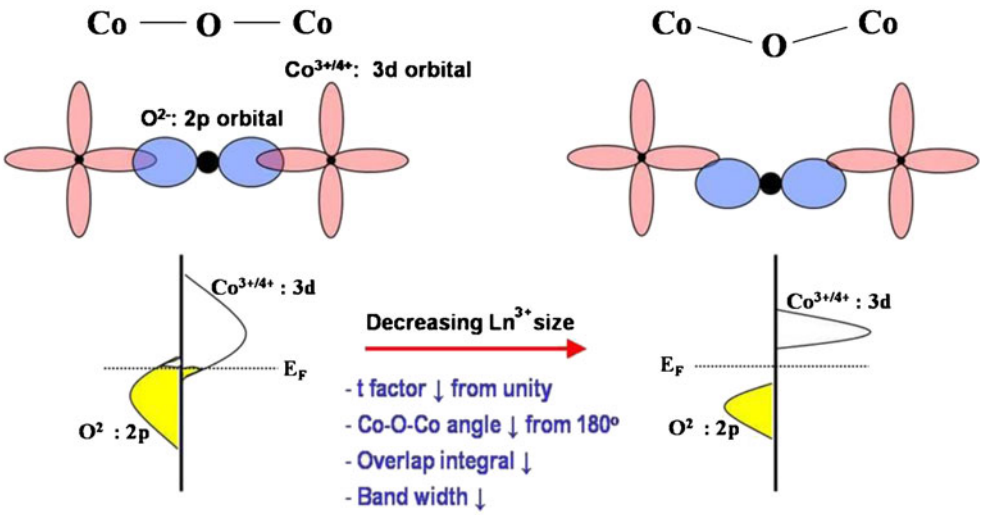

Fig. 5 Illustration of the relationship between the crystal structure and energy band diagram of the $(Ln,Sr)CoO_{3-\delta}$ perovskite oxides. As the size of the Ln^{3+} ions decreases, the tolerance factor t, O-Co-O bond angle, overlap integral, and bandwidth W decrease

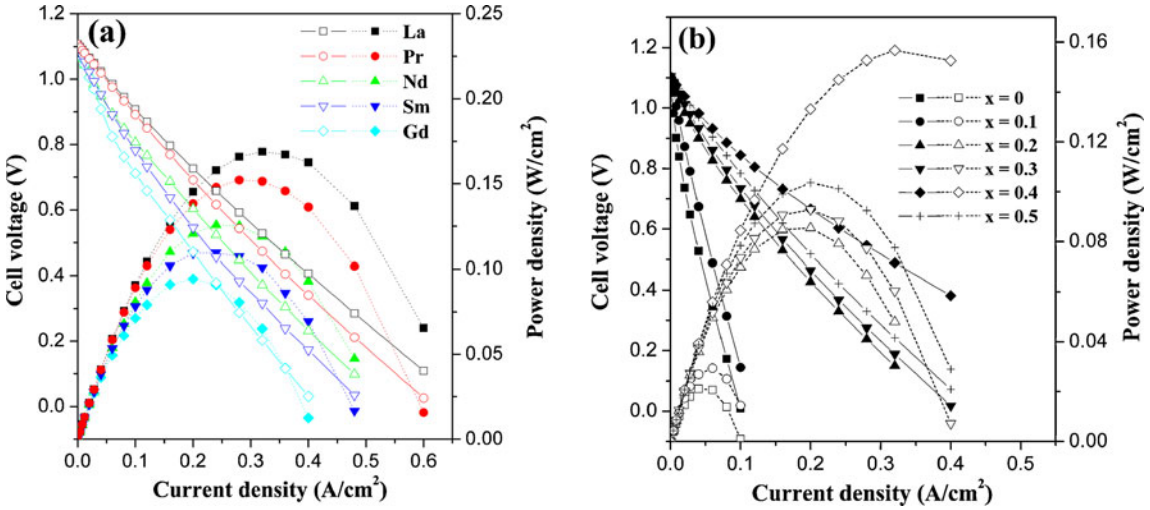

Fig. 6 Electrochemical performance data of the (**a**) $Ln_{0.6}Sr_{0.4}CoO_{3-\delta}$ (Ln = La, Pr, Nd, Sm, and Gd)/LSGM/Ni-GDC and (**b**) $Nd_{1-x}Sr_xCoO_{3-\delta}$/LSGM (thickness=1.0 mm)/Ni-GDC single cells at 800°C [31, 33]

TEC from Ln = La (21.3×10^{-6}°C^{-1}) to Gd (17.1×10^{-6}°C^{-1}) measured in the temperature range of 25–800°C in air. Generally, ionic bonds have a larger thermal expansion than covalent bonds, so the variations in TEC could be explained by considering the changes in the character of the Ln–O bonds [31, 33]. For example, Mori et al. [39] have discussed the variations in the TECs of the analogous $La_{1-x}A_xMnO_3$ (A = alkaline-earth) in terms of the ionic character of the A–O bond. A decrease in the ionic character of the Ln-O bond from Ln = La to Gd due to the decreasing electronegativity of Ln leads to a decrease in TEC. Additionally, the decreasing degree of oxygen loss with decreasing size of the Ln^{3+} ions from Ln = La to Gd due to an increasing (Ln, Sr)–O bond energy also lowers the TEC values.

However, the TEC values of the $Ln_{1-x}Sr_xCoO_{3-\delta}$ oxides even with the smaller Ln^{3+} ions are still large for SOFC applications. With an aim to lower the TEC, substitution of other transition metal ions like Mn, Fe, and Ni for Co has been investigated. Such substitutions in fact decrease the TEC values since the high-spin $Mn^{3+}(t_{2g}^3e_g^1)$, high-spin $Fe^{3+}(t_{2g}^3e_g^2)$, and low-spin $Ni^{3+}(t_{2g}^6e_g^1)$ ions do not undergo spin-state transitions on heating to high temperatures. In addition, Mn and Fe substitutions provide a stronger binding of the oxygen to the lattice, resulting in a decrease in the amount of oxygen loss from the lattice at high temperatures and minimal changes in the sizes of the B cations [40, 41]. For instance, the TGA plots (recorded in air) of the $Nd_{0.6}Sr_{0.4}Co_{1-y}M_yO_{3-\delta}$ (M = Fe and Mn) system in Fig. 7 illustrates the decrease in the amount of oxygen loss with increasing M. Accordingly, the literature data on various $Ln_{1-x}Sr_xCo_{1-y}M_yO_{3-\delta}$ (M = Mn, Fe, and Ni) perovskite systems reveal a general trend of a decrease in the TEC values with increasing amount (y) of substitution of M [14, 40–43].

At a given temperature, the electrical conductivity decreases with increasing Fe and Mn contents in (Ln,Sr) $Co_{1-y}M_yO_{3-\delta}$ (M = Fe and Mn). For example, the temperature dependence of the electrical conductivity of the $Nd_{0.6}Sr_{0.4}Co_{1-y}M_yO_{3-\delta}$ (M = Fe and Mn) systems is shown in Fig. 8 [40, 41]. The $Nd_{0.6}Sr_{0.4}Co_{1-y}M_yO_{3-\delta}$ (M = Fe and Mn) samples exhibit mixed hopping conduction with more than one type of transition metal ions, and the charge compensation on replacing Nd^{3+} by Sr^{2+} can occur by the formation of Co^{4+} or M^{4+} or both. It has been reported that the electronic charge compensation mechanism occurs preferentially by the formation of Fe^{4+} and Mn^{4+} rather than Co^{4+} in, respectively, $La_{1-x}Sr_xCo_{1-y}Fe_yO_{3-\delta}$ and $Pr_{1-x}Sr_xCo_{1-y}Mn_yO_{3-\delta}$ [42, 44]. This suggests that a preferential electronic charge compensation by $Mn^{3+}\rightarrow Mn^{4+}$ or $Fe^{3+}\rightarrow Fe^{4+}$ over that of $Co^{3+}\rightarrow Co^{4+}$ could take place in $Nd_{0.6}Sr_{0.4}Co_{1-y}M_yO_{3-\delta}$ as well. Thus, the formation of M^{4+} (M = Fe and Mn) rather than Co^{4+} decreases the covalency of the M^{4+}-O bond compared to that would be expected with the Co^{4+}-O bond, and thereby causes an increase in electron localization and a decrease in the electrical conductivity with increasing Fe or Mn content. In addition, the substitution of Fe or Mn for Co in $Nd_{0.6}Sr_{0.4}Co_{1-y}M_yO_{3-\delta}$ leads to a metal to semiconductor transition due to the changes in the crystal chemistry [33]. The substitution of a lager M^{3+} (M = Fe and Mn) for Co^{3+} results in a decrease in the tolerance factor *t* and an increased bending of the O-(Co,M)-O bonds (decrease in bond angle below 180°). The resulting decrease in the overlap integral between the $M^{3+/4+}$:3d and O^{2-}:2p orbitals and the bandwidth W leads to an opening of the charge transfer gap and a consequent metal to semiconductor transition. In addition, the ionic conductivity and oxygen permeability decrease with the substitutions of Fe or Mn [7,

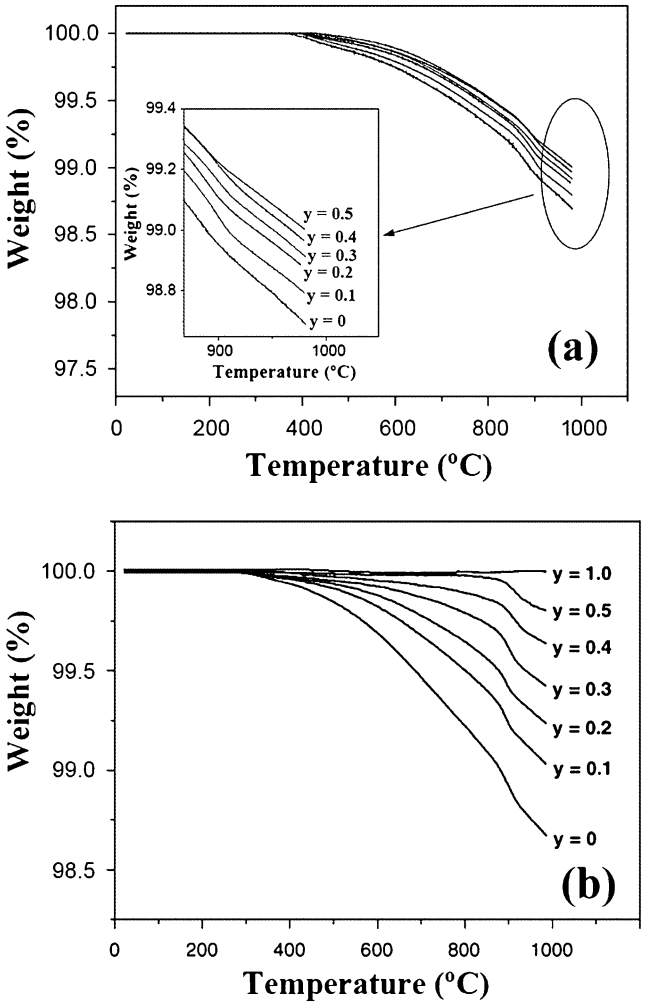

Fig. 7 Comparison of the TGA plots of (**a**) $Nd_{0.6}Sr_{0.4}Co_{1-y}Fe_yO_{3-\delta}$ and (**b**) $Nd_{0.6}Sr_{0.4}Co_{1-y}Mn_yO_{3-\delta}$ recorded in air [40, 41]

8, 14, 45] due to a stronger binding of oxygen to Fe and Mn. Since the oxygen bulk diffusion occurs via a vacancy transport mechanism in the perovksite oxides, the decreasing oxygen permeability is caused by the decreasing amount of oxide-ion vacancies on substituting Fe and Mn.

3 A-site ordered layered $LnBaM_2O_{5+\delta}$ perovskite oxides

The $LnBaM_2O_{5+\delta}$ (Ln = lanthanides and M = Co and Fe) layered perovskite oxides have an ordering of the A-site cations where the Ln-O and Ba-O layers alternate along the *c*-axis as shown in Fig. 9. The structure-magnetic property relationship of various $LnBaM_2O_{5+\delta}$ (Ln = Pr, Nd, Sm, Eu, Gd, Tb, Dy, Ho, and Y, M = Co and Fe) oxides have been investigated extensively in recent years [37, 46–49]. An interesting feature of these layered perovskite oxides is the wide variation in oxygen content with a range of $0 \leq \delta \leq 1.0$. It has been observed that the oxide-ion vacancies are localized in the LnO layers due to the preference for lower oxygen coordination of the smaller Ln^{3+} ions compared to that of the larger Ba^{2+} ion, which results in the formation of chains of CoO_5 square pyramids and CoO_6 octahedra [46, 47].

Figure 10 shows an interesting linear relationship between the room-temperature oxygen content $(5+\delta)$ and the difference in ionic radii between the Ba^{2+} and Ln^{3+} ions ($r_A{}^{2+} - r_{Ln}{}^{3+}$) for the $LnBaCo_2O_{5+\delta}$ samples synthesized in air [50]. In addition, the oxygen content values of these layered perovskite samples vary greatly depending on the pO_2 and temperature. For example, Frontera et al. [51] have reported the variation of oxygen content and crystal structure with temperature and pO_2 for the $PrBaCo_2O_{5+\delta}$ system. Among the various $PrBaCo_2O_{5+\delta}$ with different oxygen content (δ), ordering of the oxide-

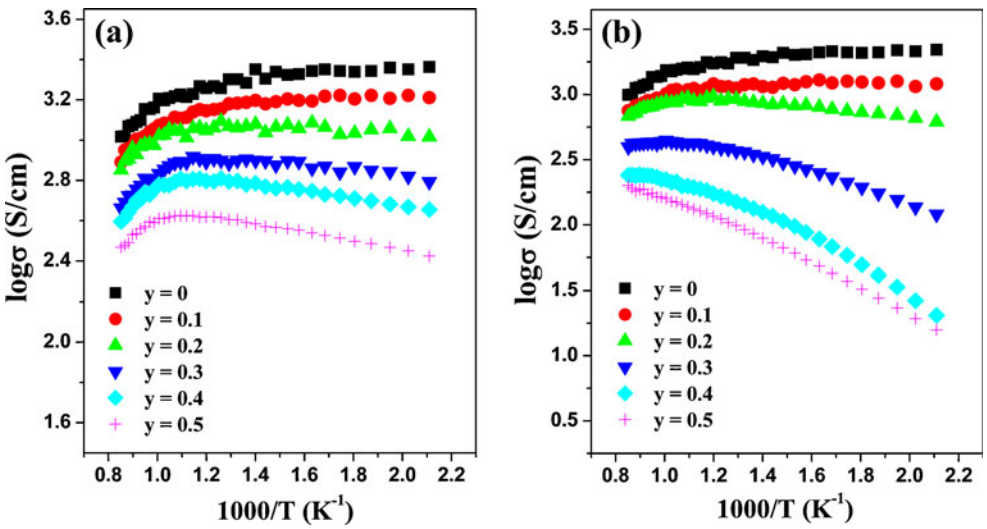

Fig. 8 Variations of the electrical conductivity measured in air with temperature: (**a**) $Nd_{0.6}Sr_{0.4}Co_{1-y}Fe_yO_{3-\delta}$ and (**b**) $Nd_{0.6}Sr_{0.4}Co_{1-y}Mn_yO_{3-\delta}$ [40, 41]

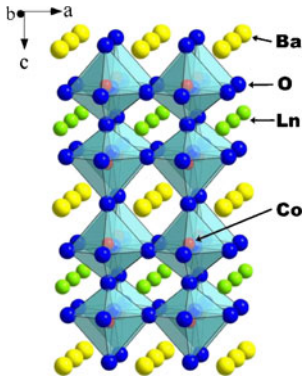

Fig. 9 Crystal structure of the A-cation ordered $LnBaCo_2O_{5+\delta}$ [19]

ion vacancies in the Pr-O layers was observed for the samples with $\delta \sim 0.75$ and 0.5, and the oxide-ion vacancy ordering was found to be lost for $\delta \sim 0.87$ and 0.18 at room-temperature. Additionally, Streule et al. [52] have reported the effect of heating on the oxide-ion vacancy order–disorder transition in $PrBaCo_2O_{5.48}$. The $PrBaCo_2O_{5.48}$ sample has an orthorhombic structure with the oxide-ion vacancy ordering at room temperature, but loses that ordering at $T > 780$ K as evidenced by a transition from orthorhombic to tetragonal symmetry measured with high-temperature neutron diffraction. This thermally activated order–disorder transition has also been observed for the Ln = Nd, Sm, and Gd samples in the $LnBaCo_2O_{5+\delta}$ [53, 54] system. For example, the high-temperature X-ray diffraction (XRD) patterns of the $NdBaCo_2O_{5+\delta}$ system in Fig. 11 indicate the order–disorder transition and the associated change from orthorhombic to tetragonal symmetry at around 500°C [53].

Several $LnBaCo_2O_{5+\delta}$ (Ln = lanthanide) layered perovskite oxides have been found to exhibit metal-insulator (M-I) transitions due to the transition of the Co^{3+} ions in octahedral-sites from low-spin $\left(t_{2g}^6 e_g^0\right)$ to high-spin $\left(t_{2g}^5 e_g^1\right)$ state [37, 48]. This M-I transition becomes less pronounced or suppressed with increasing size of the Ln^{3+} ions due to the increasing oxidation state of cobalt and the consequent decrease in oxide-ion vacancy concentration and increase in

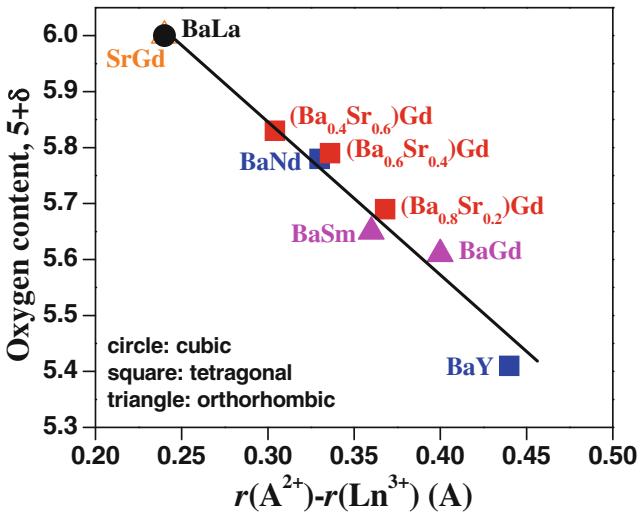

Fig. 10 Variation of the room-temperature oxygen content $(5+\delta)$ values with the difference in ionic radii between $(Ba_{1-x}Sr_x)^{2+}$ and Ln^{3+} ($r_A{}^{2+} - r_A{}^{3+}$) in the $Gd(Ba_{1-x}Sr_x)Co_2O_{5+\delta}$ and $LnBaCo_2O_{5+\delta}$ (Ln = La, Nd, Sm, Gd, and Y) samples synthesized in air. The different symbols refer to different crystal structures: *white circle*: cubic (*Pm*-3*m*), *black square*: tetragonal (*P*4/*mmm*), *black triangle*: orthorhombic (*Pmmm*), *white triangle*: orthorhombic (*Pnma*) [50]

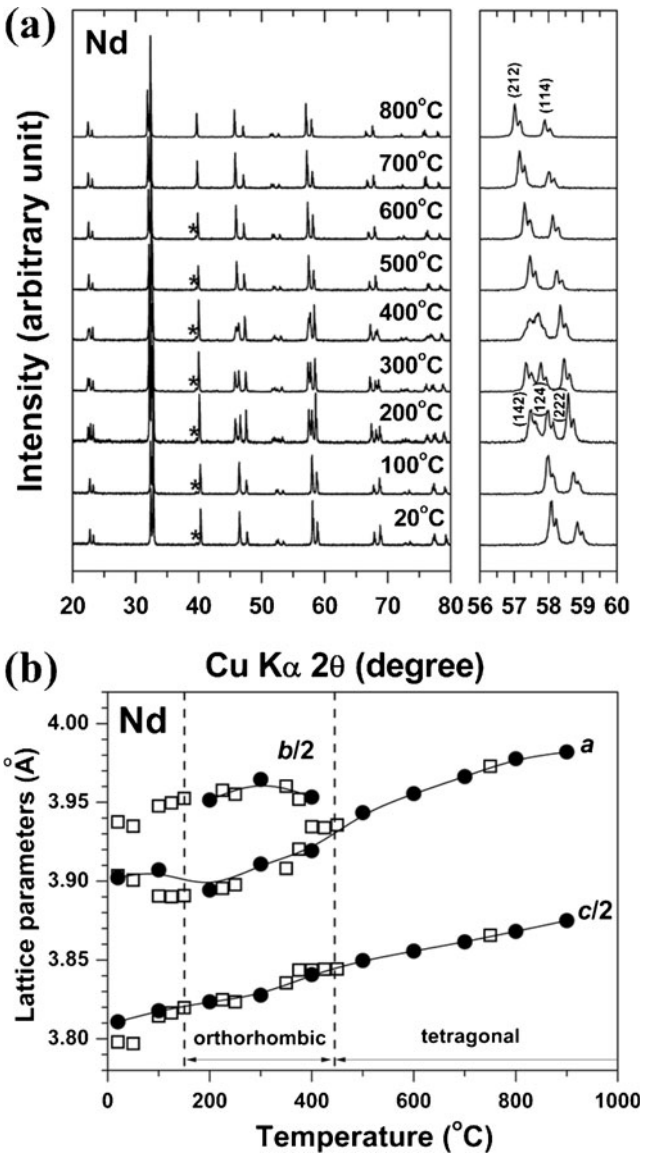

Fig. 11 (**a**) High-temperature XRD patterns of $NdBaCo_2O_{5+\delta}$ recorded with increasing temperature in air. An expanded view in the range of $56° \le 2\theta \le 60°$ is displayed in the right panel. Reflections marked with * belong to Pt from the sample stage. (**b**) Variations of the lattice parameters of $NdBaCo_2O_{5+\delta}$ with temperature. The data were collected during heating (*closed symbol*) and cooling (*open symbol*) in air [53]

the Co-O covalency and bandwidth; for example, the M-I transition is less pronounced for Ln = Pr and Nd and finally disappears for Ln = La.

The promising MIEC properties of the $LnBaCo_2O_{5+\delta}$ layered perovskite system have stimulated the exploration of their application as cathodes in SOFC. Chang et al. [55] introduced $GdBaCo_2O_{5+\delta}$ as a potential candidate for the cathode in SOFC. Taskin et al. [56] reported higher oxygen transport behavior in the layered $GdBaMn_2O_{5+\delta}$ compared to that in the disordered $Gd_{0.5}Ba_{0.5}MnO_{3-\delta}$ pervoskite. In addition, the oxide-ion diffusion and surface exchange kinetics of $LnBaCo_2O_{5+\delta}$ (Ln = Pr and Gd) have been measured using $^{18}O/^{16}O$ isotope exchange depth profile, and the results showed values comparable to those of disordered perovskite oxides [18, 57].

Our group has recently investigated the MIEC properties and the cathode performance in intermediate-temperature SOFC of several $LnBaCo_2O_{5+\delta}$ (Ln = La, Nd, Sm, and Gd) oxides. Figure 12 shows that the total electrical conductivity decreases with decreasing size of the Ln^{3+} ions from Ln = La to Y due to an increasing concentration of oxygen vacancies (Fig. 10) and a consequent decrease in the Co-O covalence and increase in the carrier localization [19]. In addition, the oxide-ion conductivity decreases with decreasing size of the Ln^{3+} ions from Ln = La to Nd to Sm, which is believed to be due to the increasing lattice strain at high temperatures [53]. However, the surface exchange rate will be an important factor in order to be a cathode in SOFC, so control of the particle size in the submicron size range to offer the necessary large surface area will be critical.

The chemical stability of cathodes in contact with the electrolyte materials is an important issue because the reaction products formed at the cathode-electrolyte interfaces are commonly poor conductors and consequently lead to increased cathode polarization resistance. In this regard, the chemical stabilities of the $LnBaCo_2O_{5+\delta}$ cathodes have been tested against standard electrolyte materials such as YSZ, LSGM, and GDC. Although all the $LnBaCo_2O_{5+\delta}$ were unstable against YSZ at high temperatures, they exhibit different chemical stability behaviors with LSGM or GDC depending on Ln. For instance, the Ln = La, Nd,

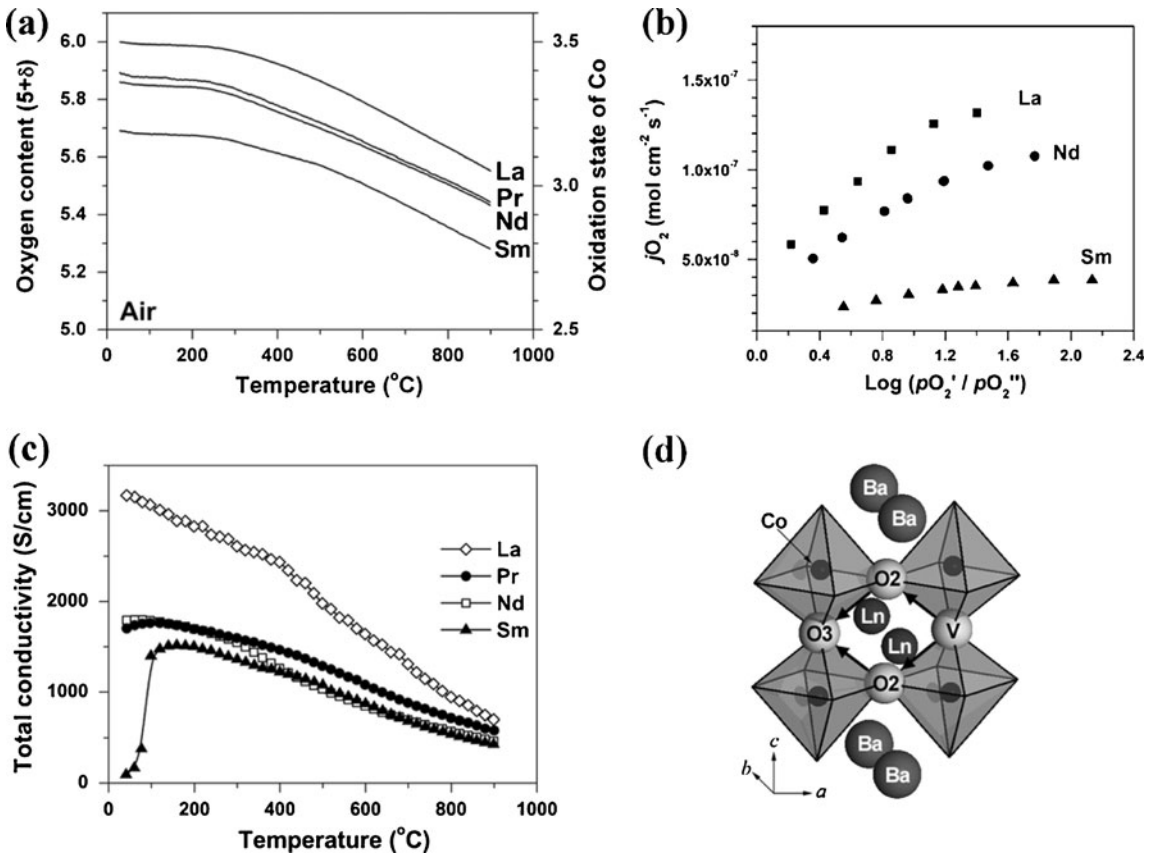

Fig. 12 Variations of the (**a**) oxygen content and the oxidation state of cobalt with temperature, (**b**) oxygen permeation flux (jO_2) of $LnBaCo_2O_{5+\delta}$ (Ln = La, Nd, and Sm) with $\log(pO_2'/pO_2'')$ at different temperatures, measured with 1.1 mm thick samples, (**c**) total electrical conductivity of $LnBaCo_2O_{5+\delta}$ (Ln = La, Pr, Nd, and Sm) with temperature in air, and (**d**) illustration of the oxygen vacancy transport in the $LnBaCo_2O_{5+\delta}$ lattice with the tetragonal structure (*P*4/*mmm*). In (**d**), the atomic positions are Ln (0,0,1/2), Ba (0,0,0), Co (1/2,1/2,*z*), O1 (1/2,1/2,0), O2 (1/2,0,*z*), and O3 (1/2,1/2,1/2), V refers to oxide-ion vacancy, the arrows indicate their hopping direction toward a neighboring site (O3), and some of the atoms are omitted for simplicity [53]

and Sm samples are stable against LSGM electrolyte while the Ln = Gd and Y show severe side reactions as evidenced by the XRD measurements after heating at 1000–1100°C [19]. Similarly, the Ln = La and Nd samples are stable against GDC, while the Ln = Gd and Y samples show severe side reactions [50]. These results suggest that the chemical stability of the $LnBaCo_2O_{5+\delta}$ cathodes against the LSGM and GDC electrolytes at high temperatures deteriorates with decreasing size of the Ln^{3+} ions.

To improve the chemical stability and the cathode performance, $Ln(Ba_{1-x}Sr_x)Co_2O_{5+\delta}$ layered perovskite cathodes have been recently investigated [50]. For instance, the $GdBa_{1-x}Sr_xCo_2O_{5+\delta}$ cathode is stable against LSGM and GDC electrolytes after heating at 1100°C [50] although the Sr-free $GdBaCo_2O_{5+\delta}$ reacts. The structural refinement results show that the Sr^{2+} ions occupy the Ba^{2+} sites, preserving largely the A-site cationic ordering. However, the oxygen content increases with decreasing size difference between $(Ba_{1-x}Sr_x)^{2+}$ and Ln^{3+} as seen in Fig. 10. With increased electrical conductivity and lower lattice strain, the $GdBa_{0.4}Sr_{0.6}Co_2O_{5+\delta}$ cathode offers better performance in SOFC compared to the Sr-free sample. Similarly, $SmBa_{0.5}Sr_{0.5}Co_2O_{5+\delta}$ has also been shown recently to exhibit better performance in SOFC [58].

In addition, several groups have recently focused on the B-site substitution in the $LnBaCo_2O_{5+\delta}$ system to obtain better thermal and electrochemical properties in SOFC. The substitution of other transition metals such as M = Fe, Ni, and Cu for Co in $LnBa(Co_{1-y}M_y)_2O_{5+\delta}$ decreases the TEC, while maintaining good cathode performance [59–62]. However, the optimum chemical composition for application in SOFC and the details of their oxygen transport mechanisms remain to be established with future studies.

4 Perovskite-based $(La,Sr)_{n+1}M_nO_{3n+1}$ intergrowth oxides

Another class of materials that have drawn attention as MIECs is the perovskite-related intergrowth oxides belonging to the Ruddlesden-Popper (R-P) series [63] having the general formula $A_{n+1}B_nO_{3n+1}$ or $(AO)(ABO_3)_n$ with A = alkaline earth or lanthanide and n=1, 2, 3. These intergrowth oxides have rock-salt AO layers alternating with a single (n=1), double (n=2), or triple (n=3) perovskite $(ABO_3)_n$ layer along the c axis [20, 64]. Figure 13 illustrates the crystal structures of the $A_{n+1}B_nO_{3n+1}$ (n=1, 2, 3) R-P systems in comparison with the ABO_3 disordered perovksite (n=∞). Among the various compositions investigated in the R-P systems (A = Ln and Sr and B = Mn, Fe, Co, Ni, and Cu), the n=1 member $La_2NiO_{4+\delta}$ has attracted great interest because of its high oxygen bulk diffusion rate comparable to that in the $La_{1-x}Sr_xCo_{1-y}Fe_yO_{3-\delta}$ perovskites and a low TEC of ~$12\times10^{-6}°C^{-1}$ compatible with those of standard electro-

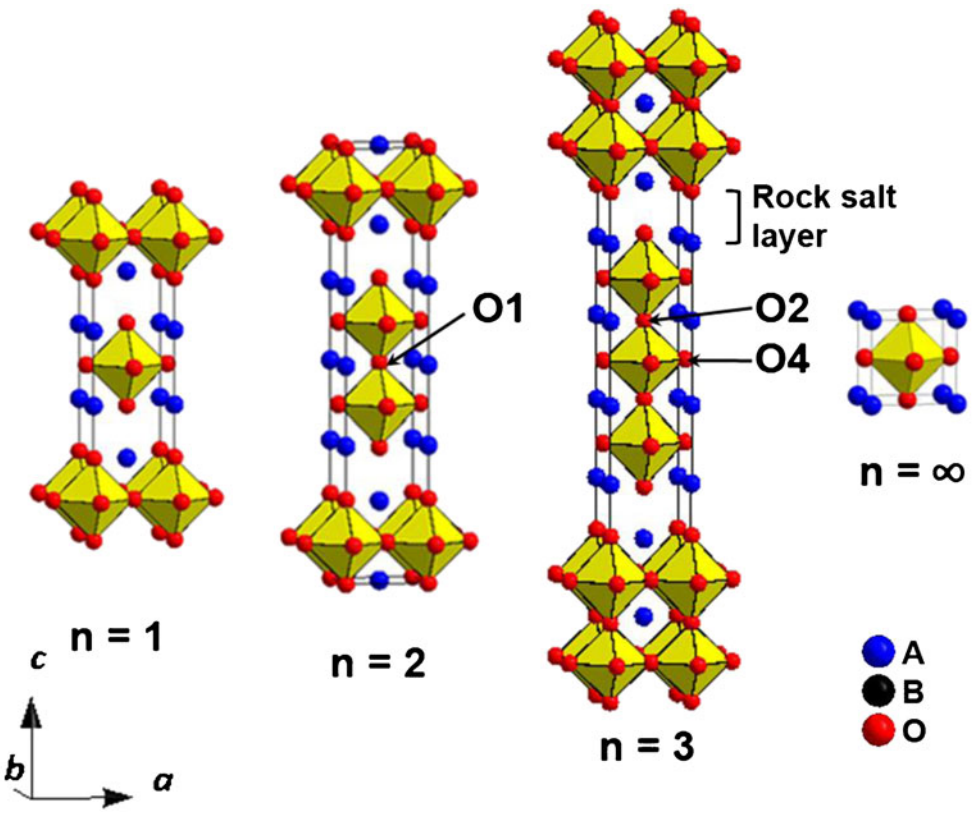

Fig. 13 Crystal structure of $A_{n+1}B_nO_{3n+1}$ (n=1, 2, and 3) Ruddlesden-Popper series of intergrowth oxides in comparison with ABO_3 perovskite (n=∞)

lytes [65, 66]. The excess δ oxygen in $La_2NiO_{4+\delta}$ is reported to be due to the incorporation of interstitial oxide ions into the rock salt layers [66]. However, $La_2NiO_{4+\delta}$ with a $Ni^{2+/3+}$ couple exhibits rather low electronic conductivity. In contrast, the n=2 and 3 members with the $Fe^{3+/4+}$ and Co^{3+4+} couples offer much higher electronic conductivities due to an increased O-B-O interaction along the c axis and a smaller charge transfer gap between the $Fe^{3+/4+}$:3d or Co^{3+4+}:3d band and the O^{2-}:2p band [20, 67–71]. With this perspective, the MIEC properties of the $(Sr,La)_{n+1}(Fe,Co)_nO_{3n+1}$ (n=2 and 3) intergrowth oxides have been extensively investigated.

The SrO – Fe_2O_3 binary phase diagram [72] in Fig. 14 indicates that the n=1–3 members of the $Sr_{n+1}Fe_nO_{3n+1}$ intergrowth oxides exhibit superior phase stability up to ~1500°C compared to other phases including the $SrFeO_{3-\delta}$ perovskite. The substitutions of La for Sr and Co for Fe in $(Sr_{1-x}La_x)_{n+1}(Fe_{1-y}Co_y)_nO_{3n+1}$ offer advantages such as improved MIEC properties (n=2 and 3), stability against moisture in air (n=2), and formation of single-phase materials without impurities (n=3). The $(Sr_{1-x}La_x)_3(Fe_{1-y}Co_y)_2O_{7-\delta}$ (n=2) and $(Sr_{1-x}La_x)_4(Fe_{1-y}Co_y)_3O_{10-\delta}$ (n=3) systems have limited solubility for La or Co while maintaining phase-pure tetragonal structure with the space group $I4/mmm$. Both the n=2 and 3 R-P systems have significant amount of oxide-ion vacancies at high temperatures without undergoing phase changes. Neutron powder diffraction studies have shown that the oxide-ion vacancies in the n=2 and 3 R-P systems are localized within the perovskite layers, *i.e.* in the O1-sites in $Sr_3Fe_2O_{7-\delta}$ and O2/O4-sites in $(LaSr_3)Fe_3O_{10-\delta}$ (Fig. 13) [73].

Considering the significant amount of oxide-ion vacancies, the oxygen transport within the systems is believed to occur by oxide-ion vacancy mechanism analogous to that in the disordered perovskite systems. The oxygen permeation data of the $Sr_{2.7}La_{0.3}Fe_{1.4}Co_{0.6}O_{7-\delta}$ membranes reveal that the oxygen transport is bulk limited rather than surface-exchange limited in the measured sample thickness range of $0.69 \le L \le 2.25$ mm [67]. Figure 15 compares the total electrical conductivities and oxygen permeation fluxes of selected $(Sr_{1-x}La_x)_{n+1}(Fe_{1-y}Co_y)_nO_{3n+1}$ samples. The results show a trend of increasing electronic and ionic conductivities from n=1 to n=∞ ($SrCo_{0.8}Fe_{0.2}O_{3-\delta}$ perovskite) in the $(Sr_{1-x}La_x)_{n+1}(Fe_{1-y}Co_y)_nO_{3n+1}$ system. The MIEC properties of the $(Sr_{1-x}La_x)_{n+1}(Fe_{1-y}Co_y)_nO_{3n+1}$ system improves with increasing n due to the increasing number (n) of $(Sr_{1-x}Ln_xFe_{1-y}Co_yO_3)$ perovskite layers (Fig. 13), resulting in

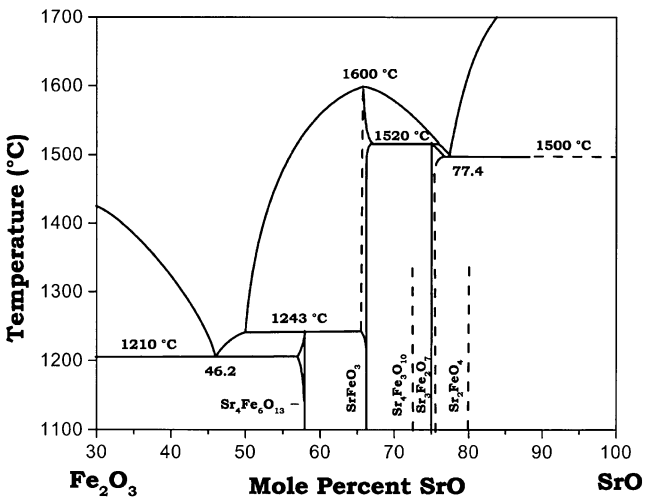

Fig. 14 Phase diagram of the SrO–Fe_2O_3 binary system [72]

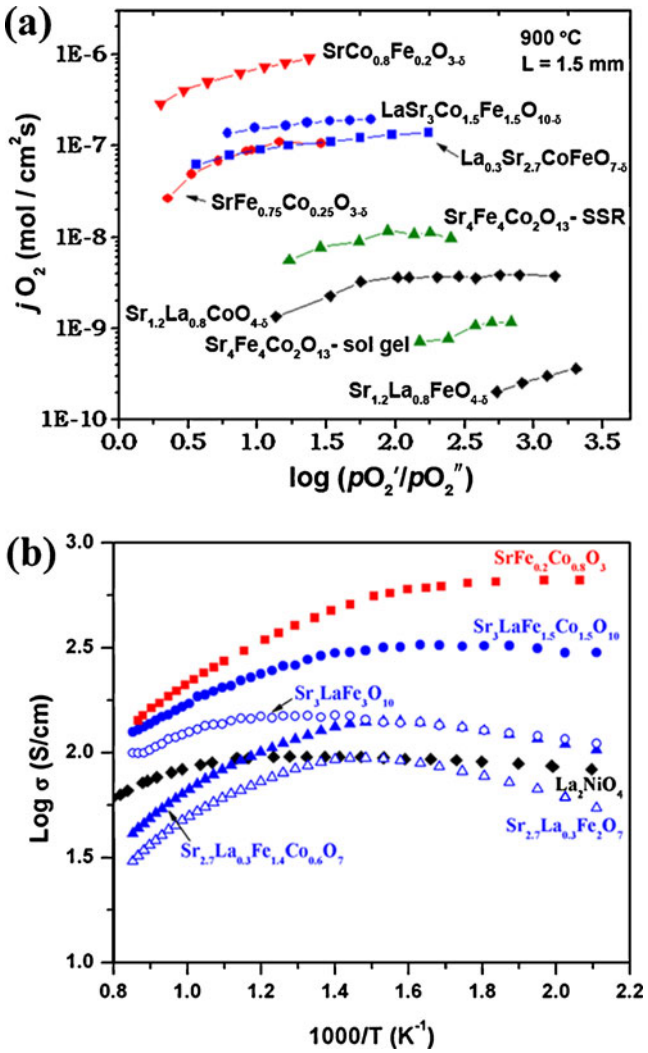

Fig. 15 (**a**) Comparison of the variations of the oxygen permeation flux jO_2 of selected intergrowth oxides with $\log(pO_2'/pO_2'')$ at 900°C with that of the perovskite phases $SrFe_{1-x}Co_xO_{3-\delta}$ having x=0.25 and 0.8. The measurements were carried out with 1.5 mm thick samples. The abbreviations ssr and sol–gel refer, respectively, to samples prepared by solid-state and sol–gel procedures. (**b**) Comparison of the variations of the total electrical conductivity of selected intergrowth oxides with temperature. Here, the data of $LaNiO_4$ is from [65]

an increasing (Fe,Co)-O-(Fe,Co) interaction and consequent electronic and ionic transport along the *c* axis within the perovskite layers. The n=1–3 intergrowth oxides exhibit an increase in conductivity with temperature, indicating a thermally activated semiconducting behavior. However, the conductivity decreases with increasing temperature for T>~500°C due to the increasing concentration of oxide-ion vacancies and a consequent perturbation of the O-(Fe,Co)-O interaction and carrier localization.

With the acceptable MIEC properties and good structural stabilities, the $(Sr_{1-x}La_x)_{n+1}(Fe_{1-y}Co_y)_nO_{3n+1}$ intergrowth oxides have been characterized as potential cathode materials for intermediate-temperature SOFC. The $LaSr_3Fe_{1.5}Co_{1.5}O_{10}$ sample exhibit high oxygen permeability and electrical conductivity comparable to that of the $SrCo_{0.8}Fe_{0.2}O_{3-\delta}$ perovskite (Fig. 15), while offering better structural stability without undergoing undesired phase transitions at high temperatures [20, 69]. The $(Sr_{1-x}La_x)_{n+1}(Fe_{1-y}Co_y)_nO_{3n+1}$ (n=2 and 3) cathodes are stable with GDC electrolytes while they react with LSGM and YSZ at high temperatures. The $LaSr_3Fe_{1.5}Co_{1.5}O_{10}$ cathode shows performance in SOFC comparable to that of the $La_{0.6}Sr_{0.4}CoO_{3-\delta}$ pervoskite cathode [70], measured with the LSGM electrolyte-supported single cell with a GDC buffer layer at the cathode-side. However, the TEC of the $LaSr_3Fe_{1.5}Co_{1.5}O_{10}$ cathode is too high compared to that of the standard electrolytes, and further optimization of the compositions is needed to lower the TEC. Furthermore, the $(Sr_{1-x}Ln_x)_{n+1}(Fe_{1-y}M_y)_nO_{3n+1}$ (M = transition metal and n=2 and 3) systems have been investigated to much lower extent compared to the ABO_3 perovskites, and further detailed work could lead to better performing cathodes with acceptable TECs. In addition, optimizing the micro-structure of the cathodes by employing the $(Sr_{1-x}Ln_x)_{n+1}(Fe_{1-y}M_y)_nO_{3n+1}$ + GDC composite could help to lower the TECs and improve the cathode performance.

5 Hexagonal $RBa(Co_{1-y}M_y)_4O_7$ oxides

Recently, $RBaCo_4O_{7+\delta}$ (R = Y, Ca, In, Lu, Yb, Tm, Er, Ho, and Dy) oxides with a hexagonal structure have attracted interest as potential oxygen storage materials since they absorb/desorb a large amount of oxygen ($0\leq\delta\leq1.5$) into/from the lattice at low temperatures of 200–400°C in addition to exhibiting interesting magnetic properties [74–82]. The $RBaCo_4O_7$ oxides consist of corner-shared CoO_4 tetrahedra with the Ba^{2+} and R^{n+} ions adopting, respectively, 12- and 6-fold oxygen coordinations as seen in Fig. 16 [75, 82]. Figure 17 illustrates the reversible oxygen absorption/desorption occurring with various $RBaCo_4O_{7+\delta}$ oxides. Chmaissem *et al.* [82] have recently suggested that the excess oxygen in $YBaCo_4O_{8.1}$ (δ=1.1) partly forms edge-shared CoO_6 octahedra instead of the corner-shared CoO_4 tetrahedra present in the stoichiometric $YBaCo_4O_7$ (δ=0) as seen in Fig. 18. Upon heating above T>450°C, however, the $RBaCo_4O_{7+\delta}$ oxides lose the excess oxygen (Fig. 17) and finally decomposes severely at 700–800°C, which prevents their use in high temperature devices [26, 77]. The decomposition products ($BaCoO_{3-\delta}$ and Co_3O_4) of the $YBaCo_4O_7$ sample suggest that the decomposition of $YBaCo_4O_7$ at elevated temperatures may be related to the tendency of cobalt to adopt octahedral coordination; while cobalt is present in tetrahedral coordination in $YBaCo_4O_7$, it is predominantly present in octahedral coordination in both $BaCoO_{3-\delta}$ and Co_3O_4. With an aim to overcome the phase-instability problem, our group has recently explored various $RBa(Co_{1-y}M_y)_4O_7$ (R = Y, Ca, and In and M = Zn, Al, and Fe) oxides [26]. The results indicate that the substitution of an appropriate amount of Zn for Co can stabilize the $YBaCo_4O_7$ phase due to a strong preference of the Zn^{2+} ions for tetrahedral oxygen coordination.

Although the substitution of Zn for Co in $YBaCo_{4-x}Zn_xO_7$ significantly improves the high temperature phase stability, it deteriorate the MIEC properties due to the

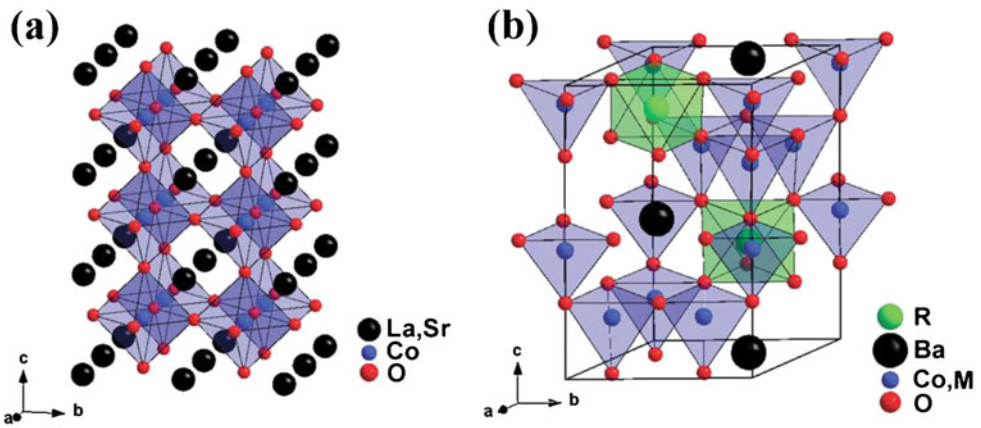

Fig. 16 (**a**) Crystal structures of perovskite $La_{1-x}Sr_xCoO_3$ and (**b**) hexagonal $RBa(Co_{1-y}M_y)_4O_7$ [26]

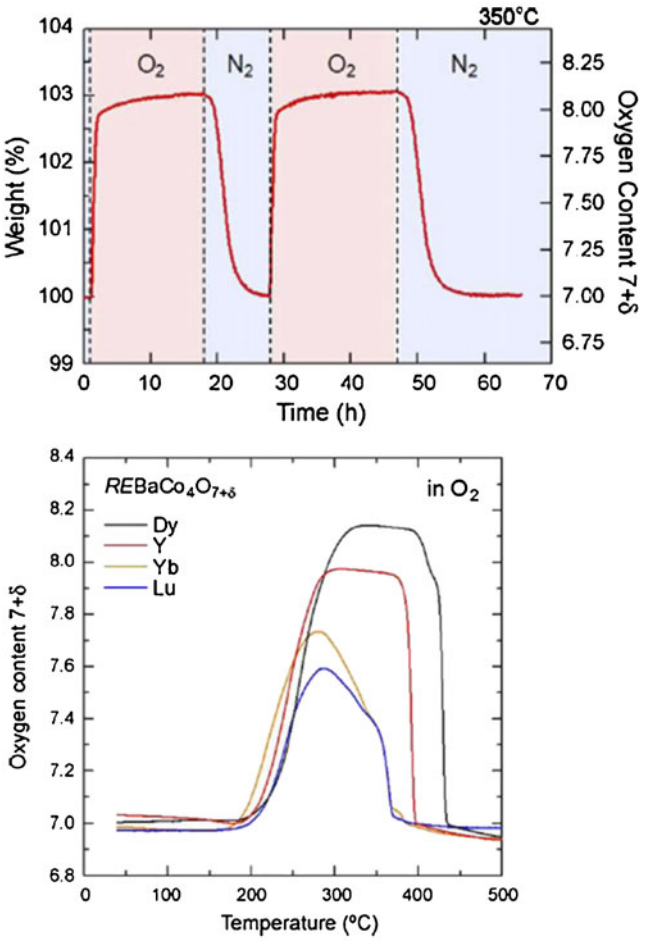

Fig. 17 Isothermal TGA curves recorded at 350°C for an as-N_2-synthesized $YBaCo_4O_7$ sample cycling in different atmospheres of O_2 and N_2 (*top*) and TGA curve of the N_2-synthesized $RBaCo_4O_7$ (R = Dy, Y, Yb, and Lu) samples in O_2 atmosphere (*bottom*) [81]

perturbation of the electron hopping pathway by the Zn^{2+} ions having a completely filled 3d orbital. For example, the $YBaCo_3ZnO_7$ sample exhibit lower oxygen permeability and electrical conductivity compared to the Co-based perovskite oxides such as $LnBaCoO_{3-\delta}$ [26]. However, our recent studies show that the $YBaCo_3ZnO_7$ + GDC composite

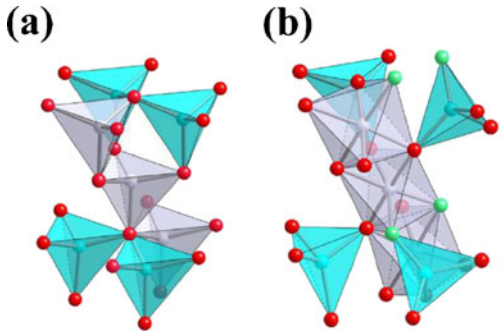

Fig. 18 Structural fragments of (**a**) $YBaCo_4O_7$ and (**b**) $YBaCo_4O_8$, illustrating the drastic displacement of some oxygen atoms and the locations of the two new oxygen atoms in $YBaCo_4O_8$ [82]

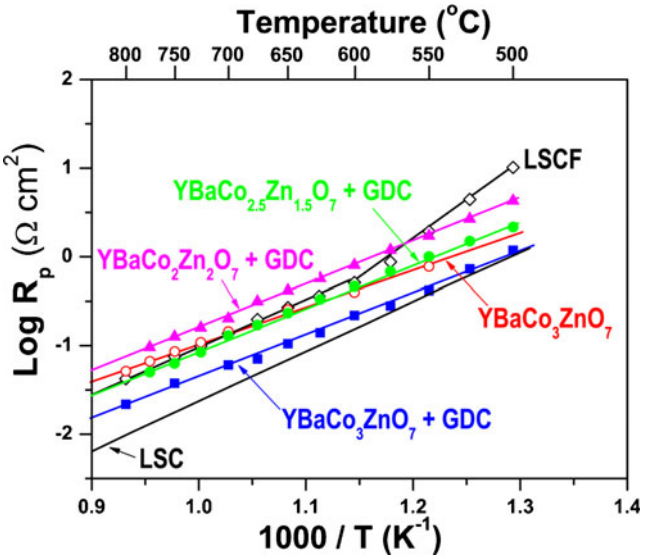

Fig. 19 Variations with temperature of the cathode polarization resistances (R_p) of the simple $YBaCo_3ZnO_7$, $YBaCo_{4-x}Zn_xO_7$ ($1.0 \leq x \leq 2.0$) + GDC composites, $La_{0.6}Sr_{0.4}Co_{0.2}Fe_{0.8}O_3$ (LSCF), and $La_{0.5}Sr_{0.5}CoO_3$ (LSC, literature data [14]) cathodes [26]

cathodes exhibit low polarization resistance and activation energy, offering better performance in SOFC compared to the $La_{0.6}Sr_{0.4}Fe_{0.8}Co_{0.2}O_{3-\delta}$ cathode (Fig. 19). The $YBaCo_3ZnO_7$ + GDC (50:50 wt.%) composite is found to be the optimum composition with the lowest polarization resistance (0.28 Ωcm^2 at 600°C) compared to the pure $YBaCo_3ZnO_7$ (0.62 Ωcm^2 at 600°C) [83]. Anode-supported single cells fabricated with the YSZ/GDC electrolyte and $YBaCo_3ZnO_7$ + GDC (50:50 wt.%) composite cathode exhibit good performance in SOFC with a maximum power density of 743 mW/cm^2 at 750°C. More importantly, the $YBaCo_3ZnO_7$ + GDC (50:50 wt.%) composite cathodes offer the critical advantage of a low TEC of 10.7×10^{-6} in the range of 20–900°C, providing good thermal expansion compatibility with the standard SOFC electrolytes. The low TECs of the $YBaCo_{4-x}Zn_xO_7$ cathodes is due to the absence of spin-state transitions with the tetrahedral-site $Co^{2+/3+}$ ions and relatively small amount of oxygen loss with increasing temperature [26, 76].

The $RBa(Co_{1-y}M_y)_4O_7$ family of cathodes is fairly new, and further work is needed to fully understand the high-temperature oxide-ion bulk transport and surface oxygen exchange mechanisms. In addition, further exploratory work could lead to high-performance SOFC cathodes and oxygen separation membranes as they offer the unique advantage of a combination of high catalytic activity for the oxygen reduction reaction and a low TEC ideally matching with that of standard electrolytes. As an example, a recent ac-impedance study has reported that the R = Tb cathode shows higher electrochemical performance compared to those obtained with the the R = Y and Er samples [84].

6 Conclusions

Over the last few decades, significant efforts have been devoted towards the exploration of MIEC oxides for high-temperature applications such as SOFC and oxygen separation membranes. Especially, major research efforts have been made on the perovskite and perovskite-related oxides due to their high electronic and oxide-ion conductivities and high catalytic activity for the oxygen reduction reaction. The MIEC properties of the perovskite oxides are strongly controlled by their chemical compositions, crystal chemistry, and chemical bonding. For instance, the electrical and ionic transport, thermal, and electrochemical properties of the $Ln_{1-x}Sr_xMO_{3-\delta}$ (M = Mn, Fe, Co, and Ni) perovskite oxides are influenced strongly by the Sr content x, size of the Ln^{3+} ions, and the nature of the M^{n+} ions. Although the cobalt-containing perovskites offer the highest catalytic activity for the oxygen reduction reaction due to the high electronic and oxide-ion conductivities, the high TEC is a major problem with them.

The perovskite-related oxides such as the A-site ordered layered $LnBaCo_2O_{5+\delta}$ (Ln = lanthanide) perovskite oxides and the Ruddlesden-Popper series of $(La,Sr)_{n+1}M_nO_{3n+1}$ (n=1–3 and M = Fe, Co, and Ni) intergrowth oxides also largely follow the trends of the disordered $Ln_{1-x}Sr_xMO_3$ perovskite oxides with respect to the transport, thermal, and electrochemical properties. However, their distinct crystal chemistry due to the cationic ordering or different structural blocks leads to some significant differences, *e.g.*, much improved structural stability without any phase transitions at elevated temperatures in contrast to the $Ln_{1-x}Sr_xMO_3$ perovskite oxides, but with a lower electronic and oxide-ion conductivities due to the reduced dimensionality (two-dimensional). The hexagonal $RBa(Co_{1-y}M_y)_4O_7$ (R = rare earth or alkaline earth and M = Zn) oxides are a fairly new family of MIEC oxides. Although they offer a unique advantage of low TEC values matching ideally with those of the standard electrolytes, the operation of the $Co^{2+/3+}$ couple instead of the more delocalized $Co^{3+/4+}$ couple in the perovskites leads to lower electronic and oxide-ion conductivities.

Acknowledgement Financial support by the Welch Foundation Grant F-1254 is gratefully acknowledged.

References

1. N.Q. Minh, T. Takahashi, *Science and technology of ceramic fuel cells* (Elsevier, Amsterdam, 1995)
2. S.C. Singhal, K. Kendall, *High temperature solid oxide fuel cells: Fundamental, design, and applications* (Elsevier Ltd., Oxford, 2003)
3. H.J.M. Bouwmeestere, A.J. Burggraaf, *The CRC handbook of solid state electrochemistry* (CRC press, New York, 1997)
4. S.P. Jiang, J. Mater. Sci. **43**, 6799 (2008)
5. H. Yokokawa, N. Sakai, T. Kawada, M. Dokiya, Solid State Ionics **40–41**, 398 (1990)
6. Y. Teraoka, H.M. Zhang, S. Furukawa, N. Yamazoe, Chem. Lett. **11**, 1743 (1985)
7. Y. Teraoka, T. Nobunaga, N. Yamazoe, Chem. Lett. **3**, 503 (1988)
8. Y. Teraoka, H. Zhang, K. Okamoto, N. Yamazoe, Mater. Res. Bull. **23**, 51 (1988)
9. J.P. Hodges, S. Short, J.D. Jorgensen, J. Solid State Chem. **151**, 190 (2000)
10. A.J. Jacobson, Chem. Mater. **22**, 660–674 (2010)
11. M.A. Señarís-Rodríguez, J.B. Goodenough, J. Solid State Chem. **118**, 323 (1995)
12. Z. Shao, S.M. Haile, Nature **431**, 170 (2004)
13. H. Ullmann, N. Trofimenco, F. Tietz, D. Stöver, A. Ahmad-Khanlou, Solid State Ionics **138**, 79 (2000)
14. C. Peters, A. Weber, E. Ivers-Tiffée, J. Electrochem. Soc. **155**, B730 (2008)
15. J.-M. Bae, B.C.H. Steele, Solid State Ionics **106**, 247 (1998)
16. E.P. Murray, M.J. Sever, S.A. Barnett, Solid State Ionics **148**, 27 (2002)
17. G. Kim, S. Wang, A.J. Jacobson, L. Reimus, P. Brodersen, C.A. Mims, J. Mater. Chem. **17**, 2500 (2007)
18. J.-H. Kim, A. Manthiram, J. Electrochem. Soc. **155**, B385 (2008)
19. A. Manthiram, F. Prado, T. Armstrong, Solid State Ionics **152–153**, 647 (2002)
20. J.A. Kilner, C.K.M. Shaw, Solid State Ionics **154–155**, 523 (2002)
21. V.M. Goldschmidt, T. Barth, G. Lunde, W. Zachariasen, Pt. VII Skrifter Norske Videnskabs-Akademi, Oslo. 117 (1926)
22. J.A. Kilner, R.J. Brook, Solid State Ionics **6**, 237 (1982)
23. R.L. Cook, A.F. Sammells, Solid State Ionics **45**, 311 (1991)
24. R.L. Cook, J.J. Osborne, J.H. White, R.C. MacDuff, A.F. Sammells, J. Electrochem. Soc. **139**, L19 (1992)
25. M. Mogensen, D. Lybye, N. Bonanos, P.V. Hendriksen, F.W. Poulsen, Solid State Ionics **174**, 279 (2004)
26. J.-H. Kim, A. Manthiram, Chem. Mater. **22**, 822 (2010)
27. H. Ullmann, N. Trofimenko, J. Alloys Compd. **316**, 153 (2001)
28. R.H. Mitchell, *Perovskites: Modern and ancient* (Almaz Press, Ontario, 2002)
29. J. Mizusaki et al., Solid State Ionics **129**, 163 (2000)
30. A.N. Petrov, O.F. Kononchuk, A.V. Andreev, V.A. Cherepanov, P. Kofstad, Solid State Ionics **80**, 189 (1995)
31. K.T. Lee, A. Manthiram, J. Electrochem. Soc. **153**, A794 (2006)
32. J. Mizusaki, Y. Mima, S. Yamauchi, K. Fueki, J. Solid State Chem. **80**, 102 (1989)
33. K.T. Lee, A. Manthiram, J. Electrochem. Soc. **152**, A197 (2005)
34. Y. Teraoka, K. Nobunaga, K. Okamoto, N. Miura, N. Yamazoe, Solid State Ionics **48**, 207 (1991)
35. V.V. Kharton, E.N. Naumovich, A.A. Vecher, A.V. Nikolaev, J. Solid State Chem. **120**, 128 (1995)
36. A.V. Kovalevsky, V.V. Kharton, V.N. Tikhonovich, E.N. Naumovich, A.A. Tonoyan, O.P. Reut, L.S. Boginsky, Mater. Sci. Eng. B **52**, 105 (1998)
37. I.O. Troyanchuk, N.V. Kasper, D.D. Khalyavin, Phys. Rev. B **58** (5), 2418 (1998)
38. M. Mori, N.M. Sammes, Solid State Ionics **146**, 301 (2002)
39. M. Mori, Y. Hiei, N.M. Sammes, G.A. Tompsett, J. Electrochem. Soc. **147**, 1295 (2000)
40. K.T. Lee, A. Manthiram, Solid State Ionics **176**, 1521 (2005)
41. K.T. Lee, A. Manthiram, J. Power Sources **158**, 1202 (2006)
42. L.W. Tai, M.M. Nasrallah, H.U. Anderson, D.M. Sparlin, S.R. Sehlin, Solid State Ionics **76**, 259 (1995)

43. M.B. Phillipps, N.M. Sammes, O. Yamamoto, Solid State Ionics **123**, 131 (1999)
44. GCh Kostogloudis, P. Fertis, Ch Ftikos, Solid State Ionics **118**, 241 (1999)
45. H.J.M. Bouwmeester, M.W. Den Otter, B.A. Boukamp, J. Solid State Electrochem. **8**, 599 (2004)
46. Y. Moritomo, M. Takeo, X.J. Liu, T. Akimoto, A. Nakamura, Phys. Rev. B **58**(20), R13–R334 (1998)
47. A. Maignan, C. Martin, D. Pelloquin, N. Nguyen, B. Raveau, J. Solid State Chem. **142**, 247 (1999)
48. T. Vogt, P.M. Woodward, P. Karen, B.A. Hunter, P. Henning, A.R. Moodenbaugh, Phys. Rev. Lett. **84**(13), 2969 (2000)
49. C. Martin, A. Maignan, D. Pelloquin, N. Nguyen, B. Raveau, Appl. Phys. Lett. **71**, 1421 (1997)
50. J.-H. Kim, F. Prado, A. Manthiram, J. Electrochem. Soc. **155**, B1023 (2008)
51. C. Frontera, A. Caneiro, A.E. Carrillo, J. Oró-Solé, J.L. García-Muñoz, Chem. Mater. **17**, 5439 (2005)
52. S. Streule, A. Podlesnyak, D. Sheptyakov, E. Pomjakushina, M. Stingaciu, K. Conder, M. Medarde, M.V. Patrakeev, I.A. Leonidov, V.L. Kozhevnikov, J. Mesot, Phys. Rev. B **73**, 094203 (2006)
53. J.-H. Kim, L. Mogni, F. Prado, A. Caneiro, J.A. Alonso, A. Manthiram, J. Electrochem. Soc. **156**, B1376 (2009)
54. A. Tarancón, D. Marrero-López, J. Peña-Martínez, J.C. Ruiz-Morales, P. Núñez, Solid State Ionics **179**, 611 (2008)
55. A. Chang, S.J. Skinner, J.A. Kilner, Solid State Ionics **177**, 2009 (2006)
56. A.A. Taskin, A.N. Lavro, Y. Ando, Appl. Phys. Lett. **86**, 091910 (2005)
57. A. Tarankon, S.J. Skinner, R.J. Chater, F.H. Ramírez, J.A. Kilner, J. Mater. Chem. **17**, 3175 (2007)
58. J.H. Kim, M. Cassidy, J.T.S. Irvine, J. Bae, Chem. Mater. **22**, 883 (2010)
59. J.-H. Kim, A. Manthiram, Electrochim. Acta **54**, 7551 (2009)
60. Y.N. Kim, J.-H. Kim, A. Manthiram, J. Power Sources **195**, 6411 (2010)
61. Q. Zhou, Y. Zhang, Y. Shen, T. He, J. Electrochem. Soc. **157**, B628 (2010)
62. S.H. Jo, P. Muralidharan, D.K. Kim, Electrochem. Commun. **11**, 2085 (2009)
63. S.N. Ruddlesden, P. Popper, Acta Crystallogr. **11**, 54 (1958)
64. F. Prado, L. Mogni, G.J. Cuello, A. Caneiro, Solid State Ionics **178**, 77 (2007)
65. V.V. Kharton, E.V. Tsipis, E.N. Naumovich, A. Thursfield, M.V. Patrakeev, V.A. Kolotygin, J.C. Waerenborgh, I.S. Metcalfe, J. Solid State Chem. **181**, 1425 (2008)
66. A. Aguadero, J.A. Alonso, M.J. Escudero, L. Daza, Solid State Ionics **179**, 393 (2008)
67. F. Prado, T. Armstrong, A. Caneiro, A. Manthiram, J. Electrochem. Soc. **148**, J7 (2001)
68. F. Prado, A. Manthiram, J. Solid State Chem. **158**, 307 (2001)
69. T. Armstrong, F. Prado, A. Manthiram, Solid State Ionics **140**, 89 (2001)
70. K.T. Lee, A. Manthiram, Chem. Mater. **18**, 1621 (2006)
71. K.T. Lee, D.M. Bierschenk, A. Manthiram, J. Electrochem. Soc. **153**, A1255 (2006)
72. P. Batti, Ann. Chim. (Rome) **52**, 941 (1962)
73. J.Y. Lee, J.S. Swinnea, H. Steinfink, W.M. Reiff, S. Pei, J.D. Jorgensen, J. Solid State Chem. **103**, 1 (1993)
74. M. Karppinen, H. Yamauchi, S. Otani, T. Fujita, T. Motohashi, Y.-H. Huang, M. Valkeapää, H. Fjellvåg, Chem. Mater. **18**, 490 (2006)
75. M. Valldor, Solid State Sci. **6**, 251 (2004)
76. A. Maignan, V. Caignaert, D. Pelloquin, S. Hébert, V. Pralong, Phys. Rev. B **74**, 165110 (2006)
77. E.V. Tsipis, V.V. Kharton, J.R. Frade, Solid State Ionics **177**, 1823 (2006)
78. H. Hao, J. Cui, C. Chen, L. Pan, J. Hu, X. Hu, Solid State Ionics **177**, 631 (2006)
79. S. Kadota, M. Karppinen, T. Motohashi, H. Yamauchi, Chem. Mater. **20**, 6378 (2008)
80. Y. Jia, H. Jiang, M. Valkeapää, H. Yamauchi, M. Karppinen, E. Kauppinen, J. Am. Chem. Soc. **131**, 4880 (2009)
81. T. Motohashi, S. Kadota, H. Fjellvag, M. Karppinen, H. Yamauchi, Mater. Sci. Eng. B **148**, 196 (2008)
82. O. Chmaissema, H. Zheng, A. Huq, P.W. Stephens, J.F. Mitchell, J. Solid State Chem. **181**, 664 (2008)
83. J.-H. Kim, Y.N. Kim, S.M. Cho, H. Wang, A. Manthiram, Electrochim. Acta **55**, 5312 (2010)
84. V.B. Vert, J.M. Serra, J.L. Jorda, Electrochem. Commun. **12**, 278 (2010)